Electron and spin transport in an ultrathin Al film

Yijia Liu [1] and R. H. Victora [1,2,*]

[1]*School of Physics and Astronomy, University of Minnesota, Minneapolis, Minnesota 55455, USA*
[2]*Department of Electrical and Computer Engineering, University of Minnesota, Minneapolis, Minnesota 55455, USA*

The effects of surface and bulk scattering on electronic and spin transport in aluminum-based ultrathin films are predicted using the Landauer-Büttiker formalism and a recursive Green's function technique. The effects of surface roughness, grain boundaries, vacancies, and surface reconstruction on resistivity, spin diffusion length, and Elliott-Yafet constant β are investigated for a 3.6-nm-thickness Al film. It is demonstrated that for a thin sputtered film, point vacancies are the dominant contribution to the momentum relaxation, and spin relaxation is dominated by the combined effect of surface reconstruction and point vacancies, which yields a reasonable spin diffusion length and the Elliot-Yafet constant. Calculations reveal that the presence of surface corrugations results in a clear departure from Matthiessen's rule and the Elliott-Yafet prediction of β, as shown by introducing random surface corrugations. It is also found that spin diffusion length induced by surface roughness is proportional to the inverse square root of the ratio between root mean square height δh and lateral correlation length ξ of a given rough surface, i.e., $(\delta/\xi)^{-1/2}$ as opposed to $(\delta/\xi)^{-1}$ as is the mean free path; this can be attributed to the interference of extended surface features.

I. INTRODUCTION

In recent years, increasing attention has been focused on the dependence of spin transport properties on sample dimension. Decreasing spin diffusion lengths with thickness have been experimentally demonstrated, even in light metals with high conductivity and weak spin-orbit interaction (SOI), such as copper and aluminum [1–6]. This slows the advance of spintronics which potentially offers a combination of desirable feature: low power consumption, fast data processing speed, and large integration densities.

Downsizing spintronic devices capable of transporting information over long distances has become crucial from both scientific and technological perspectives. In particular, non local spin valves (NLSV) are of great interest for their separation of pure spin currents from charge currents, which allows studying both spin injection and spin relaxation. In practice, it may also serve as read heads for magnetic recording [7–9] by utilizing its output originating from giant magnetoresistance (GMR) effects [10,11]. Many have been motivated to improve the head resolution and writing density by reducing the thickness of nonmagnetic materials used as transport channels, e.g., 2D materials [12–14] and light metals [15,16]. However, the output signal of NLSVs is experimentally measured to vanish quickly even with light metals as spin channels. In particular, for the thickness of a channel smaller than 10nm, the metallic spin valve performance declines substantially [17].

Many sources inducing spin relaxation have been intensively discussed in the literature. It has been suggested that extrinsic effects acting through SOI such as charged impuri-

ties and surface roughness, grain boundary (GB) scattering, and phonon scattering can be responsible for the fast spin relaxation rates in metals. Furthermore, it is expected that temperature-independent contributions, including surface and grain boundary, dominate the spin relaxation at low temperature regime. Dictated by Matthiessen's rule [18], when several different mechanisms are involved in a material, the total scattering rate $1/\tau$ is the sum of each individual one $1/\tau_i$, i.e., $1/\tau = \sum_i 1/\tau_i$, provided that the scattering events are independent [19].

Elliott-Yafet (EY) theory [20–22] is generally used to explain metallic spin relaxation with weak SOI. Based on the theory, the presence of inversion symmetry and time-reversal symmetry gives rise to a general spin state $|\tilde{\uparrow}\rangle$, which is the admixture of the two degenerate spin up ($|\uparrow\rangle$) and spin down ($|\downarrow\rangle$) states. As a result, a new pair of degenerate eigenstates are given as follows: $\Psi_{k,\tilde{\uparrow}} = (a_k |\uparrow\rangle + b_k |\downarrow\rangle)e^{ikr}$ and $\Psi_{k,\tilde{\downarrow}} = (a^*_{-k} |\uparrow\rangle - b^*_{-k} |\downarrow\rangle)e^{ikr}$, where a_k and b_k are the coefficients that preserve the periodicity of the lattice. When extrinsic sources break momentum conservation, coupled with SOI, a transition between the two degenerate spin states occurs which indicates that spin relaxation can be driven by ordinary momentum relaxation with spin-independent scattering sources, such as impurities and phonons. Furthermore, a linear relation is predicted between the spin relaxation rate τ_s^{-1} and and momentum relaxation rate τ_p^{-1}, i.e., $\tau_s^{-1} = \beta_{\mathrm{def}}^{-1}\tau_{\mathrm{def}}^{-1} + \beta_{\mathrm{ph}}^{-1}\tau_{\mathrm{ph}}^{-1}$, where τ_{def}^{-1} and $\beta_{\mathrm{def}}^{-1}$ are the momentum relaxation rates and the corresponding constant associated with defect scattering respectively and τ_{ph}^{-1} and β_{ph}^{-1} are the momentum relaxation rates and the corresponding constant due to phonon scattering respectively. β^{-1} reflects the probability of spin flips and can be used to determine the

*Corresponding author: victora@umn.edu

strength of sources inducing the spin relaxations. This relation states that defect scattering is a temperature-independent contribution to spin relaxation that can be separated from phonon scattering: their contributions to the spin relaxation can be described by $\beta_{\mathrm{def}}^{-1}$ and β_{ph}^{-1}, respectively. Using first order time-dependent perturbation theory, $\beta \approx (a_k/b_k)^2 \approx (\Delta E/\lambda_{\mathrm{SOI}})^2$, where ΔE is the average interband splitting due to SOI and λ_{SOI} is the spin orbit coupling constant. For the light metals with weak SOI, β can vary from $\sim 10^3$ to $\sim 10^5$ [4,17].

It has been proposed that when the mean free path is comparable to the dimension of metals, surface scattering should dominate over spin relaxation [15]. However, studies addressing size effects on spin relaxation mechanism in metals suggested that the dominant contribution to spin relaxation is GB scattering [4,16,23]. So far no consensus has been reached yet because GB scattering and surface scattering are generally coupled and both surface roughness and GB are strongly dependent on the growth and deposition conditions, which varies among experimental groups. Therefore the dominant contribution at low temperature to spin relaxation remains puzzling. In addition, the Fuchs [24] and Sondheimer (FS) model [25] and the Mayadas and Shatzkes (MS) [26] model, used to quantify momentum relaxations induced by surface roughness and GB scatterings respectively, are incomplete. Phenomenological parameters, such as surface specularity and the grain boundary reflection coefficient, which are fitted as free parameters or usually assigned to indicate the extreme cases, generally cannot be directly related to measured surface parameters or grain boundary structures, thus imposing challenges to determining realistic values for the parameters in the fitting.

Among metals, aluminum is an outstanding candidate for spintronic devices due to its low resistance, inherently long spin relaxation time, low cost and manufacturability. However, the study of spin relaxation induced by defects in Al is not as intensive as that in other light metals and 2D materials. It may be attributed to growth problems and existence of spin hot spots in Al. Al possesses a challenging growth problem characterized by "Hillocks." When deposited on a substrate with a low coefficient of thermal expansion (Si or SiO_2), the formation of hillocks can cause an increase in surface roughness and vacancy formation in the bulk. Hillocks appear in the surface of the metal layer due to the residual stress and strain developed during the deposition. Consequently, an increase in surface roughness is expected, which can cause an increase in strain and compressive stress [27,28]. A large compressive strain can lead to vacancy formation in metallic thin films [29]. Therefore a surprisingly large vacancy concentration can be expected at low temperature. In addition, aluminum, as a polyvalent metal, has outliers whose spin relaxation rate is at least two order of magnitude larger than k points away from the Brillouin zone boundaries [30,31]. Such outliers, called "spin hot spots," occur when the Fermi surface crosses the Brillouin zone boundaries. However, the presence of spin hot spots and vacancies in a thin film of Al with defects has not been addressed. It is thus important to exam the spin relaxation rate induced by vacancies in a thin film of Al at low temperatures and to survey the existence of spin hot spots in a defective-Al system, which otherwise produce a long spin diffusion length.

In this work, an ultrathin Al film is used to investigate the effect on the spin relaxation induced by surface roughness, GB scatterings, vacancy scatterings and surface reconstruction respectively, employing the Green's function method. Based on the Landauer-Büttiker formalism [32,33], a 3.6-nm-thick Al system is connected to two semi-infinite and translationally invariant Al leads; resistivity, mean free path, spin diffusion length and EY constant β are determined at zero temperature using the transmission function $T(E)$ which is obtained from the Green's function at the Fermi energy. Explicit contributions from grain boundaries, surface roughness and vacancies in the thin film regime are determined and compared with various experimental results. Our results can potentially widen the application of nonlocal spin valves for spintronics and magnetic recording read heads with smaller shield-shield spacing.

The article is presented by first introducing the Hamiltonian of Al as described by a tight-binding model in the presence of defects. A recursive Green's function method is presented in Sec. II, followed by discussion of the results for momentum relaxation and spin relaxation induced by surface roughness, GB scattering, vacancy scatterings, surface reconstruction and anisotropy in spin relaxation in Sec. III and a summary of the conclusions in Sec. IV.

II. METHODS

It is convenient to study the disordered systems with Green's function described by the tight-binding model [34]. The Hamiltonian of the system is described as $H = H_{\mathrm{TB}} + H_{\mathrm{SOC}}$, where H_{TB} is the Hamiltonian in the tight-binding structure with first and second nearest-neighbor hopping and H_{SOC} is the intrinsic spin-orbit interaction. H_{TB} is determined by the Slater-Koster (SK) parameters in s, p, and d orbitals [35]. A principal layer consists of two atomic layers to accommodate second-nearest-neighbor hopping given in the SK parameters. For a system with N principal layers, the general structure of H_{TB} for a given a spin state is in the block tridiagonal form as follows:

$$
\begin{bmatrix}
H_L & t_L & 0 & 0 & 0 & \ldots & 0 \\
t_L^{\dagger} & H_1 & t & 0 & 0 & \ldots & 0 \\
0 & t^{\dagger} & H_2 & t & 0 & \vdots & 0 \\
\vdots & \vdots & \ddots & \ddots & \ddots & \ldots & \vdots \\
0 & \ldots & & t^{\dagger} & H_i & t & \vdots \\
& & & 0 & t^{\dagger} & H_N & t_R \\
0 & & \ldots & & & t_R^{\dagger} & H_R
\end{bmatrix}.
\tag{1}
$$

In Eq. (1), H_L/H_R denotes the Hamiltonian of the left/right semi-infinite leads, respectively; t_R and t_L represent the interaction between the leads and layers in the scattering regions. The on-site Hamiltonian for the ith principal layer is denoted by H_i for $1 \leqslant i \leqslant N$. t is the hopping matrix between two adjacent principal layers which is identical for any two adjacent principal layers as the scattering potential only alters the on-site Hamiltonian H_i in the simulation. Each entry in Eq. (1) is a submatrix, whose dimension is determined by the number of orbitals for each Al atom and the number of atoms in one atomic layer. H_{SOC} is the spin-orbit coupling term that can be

written as

$$H_{\text{SOC}} = \lambda \hat{L} \cdot \hat{S}, \quad (2)$$

where λ is the spin-orbit coupling constant and $\lambda = 0.0018$ Ry for aluminum. $\hat{L}$ and $\hat{S}$ are angular momentum and spin operators of the system, respectively.

The general form of the retarded (advanced) Green's function $G_d^r (G_d^a)$ for a device at a given energy E can be expressed as

$$G_d^{r/a}(E) = [E \pm i\delta - H - \Sigma_L - \Sigma_R]^{-1}. \quad (3)$$

Here $\Sigma_{R/L}$ is the self-energy function of the left or right lead and δ is an infinitesimal convergence parameter. Define $\epsilon = E \pm i\delta$. Note that all the relevant quantities are evaluated at the Fermi energy with 0.002 Ry as an imaginary part for numerical convergence. The value of the imaginary convergence parameter is chosen for numerical stability with fast convergence speed. Including spin-orbit coupling, the Green's function can be written as

$$G(\epsilon) = \begin{bmatrix} G_{\uparrow\uparrow}(\epsilon) & G_{\uparrow\downarrow}(\epsilon) \\ G_{\downarrow\uparrow}(\epsilon) & G_{\downarrow\downarrow}(\epsilon) \end{bmatrix}. \quad (4)$$

The self-energy function of the left or right lead $\Sigma_{R/L,\sigma}$ with a spin state σ is defined as

$$\Sigma_{L/R,\sigma} = t_{L/R,\sigma}^\dagger g_{L/R,\sigma} t_{L/R,\sigma}, \quad (5)$$

where $g_{L/R}$ is the interface Green's function of the semi-infinite left or right lead. Assuming that the spin-flip process only occurs in the scattering channels, the transmission function that can be related to the Green's function by the *Caroli* formula [36] given by

$$T_{\uparrow\uparrow} = Tr[\Gamma_{L\uparrow} G_{\uparrow\uparrow}^r \Gamma_{R\uparrow} G_{\uparrow\uparrow}^a] \quad (6)$$

$$T_{\uparrow\downarrow} = Tr[\Gamma_{L\uparrow} G_{\uparrow\downarrow}^r \Gamma_{R\downarrow} G_{\downarrow\downarrow}^a], \quad (7)$$

where $T_{\uparrow\uparrow}$ represents the transmission function with both spin up states in the left and right lead and $T_{\uparrow\downarrow}$ represents the transmission function with opposite spin states in the left/right lead. $\Gamma_{\alpha\sigma}$ is the level width function with a spin state σ that broadens the width of energy level and is defined as

$$\Gamma_{L/R,\sigma} = i(\Sigma_{L/R,\sigma}(\epsilon) - \Sigma_{L/R,\sigma}^\dagger(\epsilon)). \quad (8)$$

Notice that direct inversion of the Hamiltonian in (1) requires the number of steps to be on the order of $O(M^3 N^3)$, where M is the number of degree of freedoms within one principal layer and N is the number of principal layers in the system. However, with Dyson's equation, one can obtain the Green's function of the system by recursively coupling one principal layer to another, which only requires one inversion of the matrix for a principal layer each time. Therefore the total number of steps required is on the order of $O(M^3 N)$. In the transport calculations, the typical number of N is on the order of 10^2. Thus the recursive method is at least four orders of magnitude faster than the direct inversion.

The interface Green's function can be obtained with an improved method of the recursive Green's function [37] by using the translational invariance of the attached leads. For each iteration, the Hamiltonian of principal layers and hopping terms are updated to couple the adjacent even layers. For the

k_{th} iteration, the layers that are the multiple of 2^k is included into the recursive relations, resulting in an exponentially fast convergent speed. The simulation is conducted under the assumption that the system is in a surrounding vacuum. Both leads and the scattering region as shown in Fig. 1, are made of a thin film of Al with 3.6nm thickness. Periodic boundary conditions are applied with wave vectors sampled along the transverse direction (in the y direction as shown in Fig. 1), which achieves convergence within 6%. The other transverse direction (in the z direction as shown in Fig. 1) is treated in real space. As a result, surface roughness can be achieved with one-dimensional surface height. For simplicity, the 1D surface height is generated by a Gaussian distribution function modulated by a Gaussian autocorrelation function with specified RMS height δh and correlation length ξ. Depending on the roughness of a surface, extra atomic layers equivalent to twice δh are preserved for atomic protrusions. A 5-Ry offset potential is added to simulate the vacuum environment and missing atoms on the surface as indicated in the yellow region of Fig. 1. To ensure the 5 Ry offset potential effectively simulates the vacuum, without introducing a repulsive effect on the surface scattering, a modulation of the onsite-energy is provided at top and bottom surface layers, maintaining the electron occupancy of these two surface layers. Grain boundary scattering is achieved by introducing grains whose size follows a log normal distribution [38]. Vacancies are introduced by adding a 1.5 Ry potential offset at the vacancy sites that is larger than the difference between the bottom of the band and the Fermi level. It is assumed that vacancies are randomly and uniformly distributed with a probability C_{vac}, which denotes the vacancy concentration. Lastly, surface reconstruction is investigated with surface corrugations with varying periods and random period, where a repeated pattern or random patterns of missing atoms are placed at the surface. All the quantities are computed by averaging over the number of defect configurations and the associated errors are determined from the standard deviation of the relevant quantities. Note that depending on the distributions followed by different types of defects, the number of defect configurations used in the simulations is deliberately chosen such that doubling the number kept the error within 5%.

III. RESULTS AND DISCUSSION

A. Surface roughness

From the transmission function predicted by the Green's function, resistivity can be obtained through $G(E) = 2e^2 T(E)/h$, where G is conductance. Assuming that the size effect on the density of states and Fermi velocity can be neglected and the Drude model for the free-electron is valid in the system with defects, then the momentum relaxation rate $\tau_p^{-1} \propto \rho$ and the mean free path is given by $\lambda_{\text{mfp}} = \sqrt{3}/\rho g e^2 v_F$, where the density of states at the Fermi level $g = 2.4 \times 10^{28}$ eV^{-1} m^{-3} and Fermi velocity $v_F = 2.03 \times 10^6$ m/s [39]. The effective mass of a 3.6-nm-thick system with defects is estimated to be $\sim$90% of the predicted values determined by the SK parameters and hence the free electron assumption will be accurate to within 10%. Spin diffusion length is
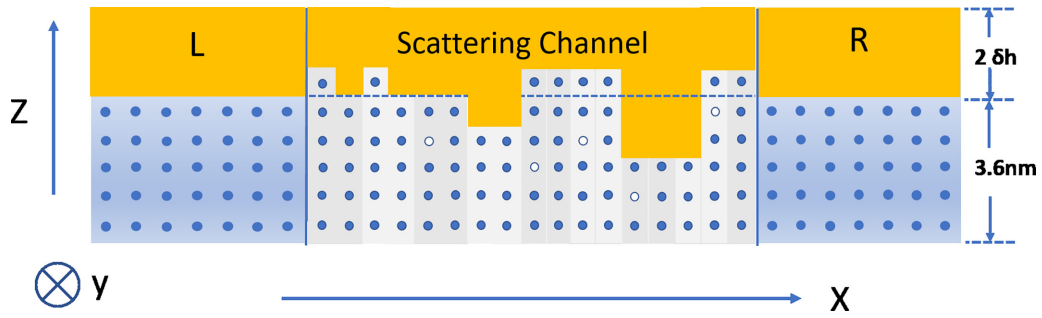
FIG. 1. Schematic of the transport model in the presence of surface roughness and vacancies. L denotes the left lead and R denotes the right lead. To simulate the surface roughness, twice of δh is included in both leads and scattering region for surface bumps. The yellow region indicates the positions with 5 Ry added to simulate the vacuum environment. The white circles represent vacancies, which is achieved with 1.5 Ry onsite-offset potential exerted. Note that the transport model shown here is for visualization and the actual dimensions and scales of each region may vary.

determined from spin polarization P, which is defined as $P = (T_{\uparrow\uparrow} - T_{\uparrow\downarrow})/(T_{\uparrow\uparrow} + T_{\uparrow\downarrow})$ and $P \propto \exp(-d/L_{sf})$ in the diffusive regime, where L_{sd} is the spin diffusion length and d is the channel length. The EY constant β is determined by $\beta = \tau_s/\tau_p = (L_{sd}/\lambda_{mfp})^2$.

As shown in Fig. 2(a), the resistivity due to surface roughness ρ_{surf} exhibits an Ohmic behavior as expected for the cases where the root mean squared height δh is below 1.0 nm and the lateral correlation length $\xi = 10$ or 20 nm. A minor tunneling effect occurs when δh is increased to 1.0 nm. The fact that an increase in resistivity and a decrease in spin diffusion length correlate to the rougher surfaces demonstrates that the surface roughness enhances the momentum and spin relaxation.

As shown in Table I, the values of resistivity scale linearly with $\delta h/\xi$, i.e., $\rho \propto \delta h/\xi$. Note that an $\sim$10% difference in ρ is observed in Table I between the case where $\delta h = 0.4$ nm and $\xi = 10$ nm and that where $\delta h = 0.8$ nm and $\xi = 10$ nm, which have the identical ratio of $\delta h/\xi$. But this difference is within the uncertainty, which increases with the surface roughness.

$\delta h/\xi$ can be understood as the average slope of the surface protrusions. An increase in $\delta h/\xi$ leads to a steeper slope of the surface bumps, which will increase the backscattered probability for electrons and hence a higher resistivity is expected. This result is consistent with the model for surface roughness scattering dependent on resistivity proposed in Ref. [40] (by Zhang *et al.*) at the sub-10nm regime of thickness. In contrast, it has been shown that treating surface roughness perturbatively in the Kubo linear response theory [23,41] brings about δh^2 dependence in resistivity, i.e., $\rho \propto \delta h^2$. This discrepancy

arises because the first order perturbation treatment on surface roughness is not well justified. In particular, at the sub-10-nm regime of film thickness where surface scattering dominates, the electron coherence length is comparable to the lateral correlation length such that the resulting wave function for the electron scattering is associated with multiple scattering events and cannot be described independently.

In order to extract the spin diffusion length, the range of the channel lengths is chosen to consistently correspond to the values of ln(P) between 0.6 and 1.0, which effectively avoids a slight curvature at a small channel length in the spin diffusion plot. The slight curvature is attributed to the contact resistance between the leads and the scattering channels and the transition between the ballistic and diffusive transport. As shown in Fig. 2(b), the linearity is restored in the chosen range of the channel lengths. It is observed that β_{surf} ranges from $\sim$300 to $\sim$1000 with the imposed surface roughness contrary to a relative constant value based on Elliott-Yafet theory. More specifically, β_{surf} shows a roughly linear dependence on $\delta h/\xi$ as well. The wide range of β_{surf} arises from the fact that the spin-flip scattering is more resilient to the variation of surface roughness compared to the momentum relaxation. It is found that the spin diffusion length is proportional to $(\delta h/\xi)^{-1/2}$ in contrast to the linear dependence on $\delta h/\xi$ of both β_{surf} and ρ_{surf} as illustrated in Fig. 3. Consequently, the corresponding spin relaxation rate is invariant with respect to $\delta h/\xi$, and the $(\delta h/\xi)^{-1/2}$ dependence of spin diffusion length is completely attributed to momentum relaxation based on $L_{sd} = \sqrt{D\tau_s}$ where the diffusion constant $D = 1/ge^2\rho$ according to the Einstein relation. Considering that the spin coherence length is appreciably larger than the characteristic size of surface bumps or dents, it is apparent that within the channel length of interest, the effective scattering potentials are the collective outcome of multiple surface features, which is likely to outweigh the spin flip scatterings induced by each individual surface feature.

Overall, the values of resistivity are in a reasonable range compared to the simulated results from Ref. [23] after scaling with respect to thickness and surface roughness parameters. Note that the simulations in this article are executed with one-sided roughness imposed rather than double-sided as in the actual experiments. Assuming the surface roughness of top and bottom interfaces are uncorrelated and independent,

TABLE I. Summary of the effect of surface roughness on electric and spin transport in a 3.6-nm-thick Al film at $T = 0$ K.

δh (nm)	ξ (nm)	ρ ($\mu\Omega$ cm)	L_{sd} (nm)	β_{surf}
0.4	20	0.42	820	248
0.4	10	0.75	731	630
0.6	20	0.67	693	452
0.8	20	0.83	645	600
1.0	20	1–1.2	583	861[a]

[a]Determined with $\rho = 1.1$ $\mu\Omega$ cm, which is the average value.
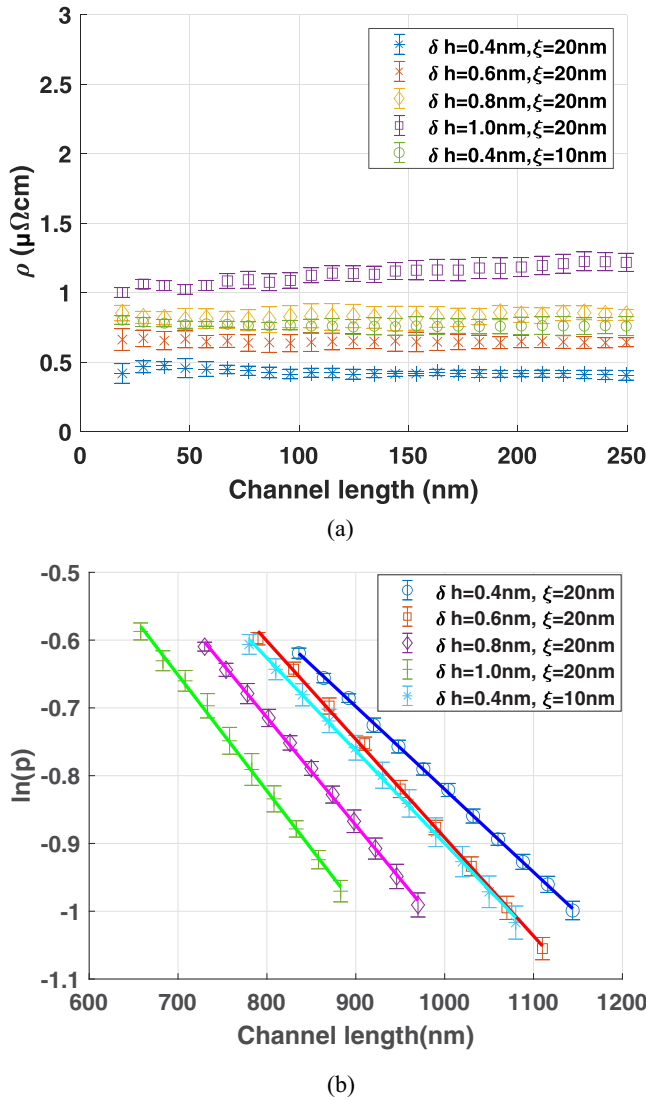
(a)

(b)

FIG. 2. (a) Resistivity of Al with 3.6 nm thickness vs channel length under different sets of surface roughness parameters. (b) Spin diffusion lengths under the same sets of roughness parameters as above. P is the spin polarization.

the resulting momentum and spin relaxation rates will be approximately doubled. However, compared to the experimental results [42–46], in particular, to that from Ref. [4], both resistivity and spin diffusion length are approximately one order of magnitude removed from the typical values for $t_N < 25$ nm when accounting for the thickness [47,48] and double-sided roughness, indicating that the dominant effect on the relaxation cannot be attributed to the surface roughness. Typically, as shown in Table VII, ρ is ~ 10 µΩ cm, L_{sd} is between 100 and 1000 nm and β is $\sim 10^4$ for 10 nm $< t_N < 20$ nm.

B. Grain boundary scattering

Several factors have been investigated for GB scattering. Grain boundary spacing follows a log-normal distribution and grain boundaries are treated as potential barriers with heights and thickness. Two GB thicknesses t_{GB}, 0.4 and 0.8 nm, are used in our simulations since typical metallic grain boundary
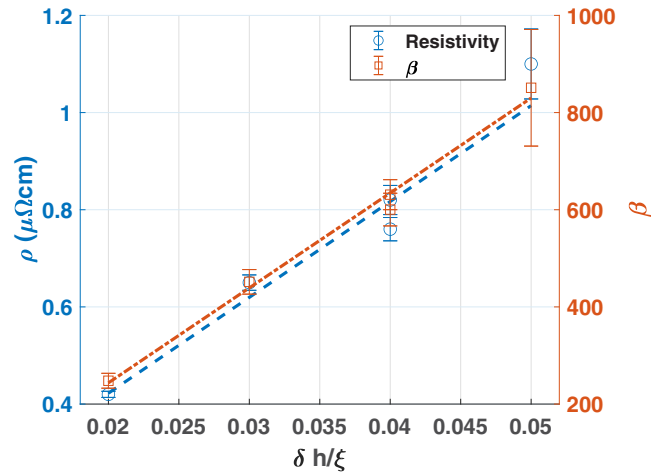

FIG. 3. Resistivity of 3.6-nm-thick film varies with $\delta h/\xi$ in blue and the corresponding β in red. The fitting dashed lines are used to show the linear trend. Note that the larger error bar for $\delta h/\xi = 0.05$ is due to the weak tunneling effect.

thickness is ~ 0.5 nm [49]. Given that the potential barrier height of the grain boundary strongly depends on the material and GB structure, two types of grain boundary barrier V_{GB} (-0.05 and -0.2 Ry) are being studied, where -0.05 Ry is a potential drop for a typical GB barrier with impurities and -0.2 Ry is a potential drop to simulate oxidized grain boundaries. The relationship between the grain size and ρ_{GB} is also examined with average grain sizes d_{GB} of 50 and 30 nm, which are realistic values measured in thin films [4]. For simplicity, only perpendicular grain boundaries are considered in the simulation.

As shown in Table II and Figs. 4(a) and 4(b), momentum and spin relaxation rates grow inversely with grain size and increase with increasing GB barrier and GB thickness, suggesting that momentum and spin relaxation are both enhanced by the grain boundaries. Note that because the spin diffusion length induced by grain boundaries is approximately two orders of magnitude larger compared to the surface-induced relaxation, available computational resources make it impossible to achieve the channel-length range corresponding to the value of $\ln(P)$ that falls between 0.6 to ~ 1.0. To be consistent, a fixed channel-length range is used from 110 to 250 nm. But compared to the resulting spin diffusion lengths, the chosen channel-length range is too small to confirm the linear behavior, causing a relatively large uncertainty on the spin diffusion length.

With the imposed practical GB parameters, the contribution of GB scattering to the momentum relaxation is generally at the same order but weaker than that of surface scattering. In addition, ρ_{GB} and L_{GB} are found to be at least one order of magnitude away from the experimental results as shown in Table VII. And β_{GB} is almost two orders of magnitude larger than β_{surf} in general, indicating that the contribution to spin relaxation induced by grain boundaries is negligible compared to that induced by surface roughness with the imposed parameters at sub-10-nm thickness. Symmetry can account for the weak momentum and spin relaxation. With the imposed grain boundaries, translational symmetry along the traverse and

TABLE II. Summary of the effect of grain boundaries on electric and spin transport in a 3.6-nm-thick Al film at $T = 0$ K.

d_G (nm)	V_{GB} (Ry)	t_{GB} (nm)	ρ (μ Ω cm)	L_{sd} (nm)	β_{GB}
30	−0.05	0.8	0.13	3.6×10^4	4.5×10^4
50	−0.2	0.4	0.23	1.6×10^4	2.8×10^4
30	−0.2	0.4	0.34	1.4×10^4	5.5×10^4
30	−0.2	0.8	0.72	0.9×10^4	8.6×10^4

thickness directions are preserved and thus momentum and spin relaxation are undermined as scatterings can only occur in the propagation direction. Overall, it is still inconclusive regarding the exact dependence of the momentum and spin relaxation on the imposed GB parameters, given a relatively large uncertainty involved in the spin relaxation and weakly scattered GB parameters imposed. However, neither surface scattering nor GB scattering seem strong enough to account for the experimental results.

C. Vacancies

So far, the effects of both surface roughness and grain boundary scattering on the properties of electron and spin transport in an Al thin film are not sufficiently strong to explain the experimental findings. Thus a new source of scattering from vacancies is studied. 2% vacancies are assumed to be uniformly distributed throughout the thin film [50]. The effects of line vacancies and point vacancies with/without surface roughness on electronic and spin transport are simulated. As shown in Fig. 5(a), a strong tunneling effect occurs in the presence of line vacancies. However, in the presence of point vacancies, ρ recovers ohmic behavior, which indicates that point vacancies are a more realistic assumption, as expected. Note that the channel length in Fig. 5(a) is extended to ∼600 nm to demonstrate the strong tunneling effect owing to the line vacancies and the ohmic character of resistivity for the point vacancies, i.e, resistivity is independent of channel length. For readability and accuracy, the resistivity for the case combining 2% line vacancies and surface roughness is only plotted to 250 nm. Hence, owing to the ohmic character of resistivity, the extraction of β with resistivity and spin diffusion length determined at different ranges of channel length is well-justified for surface roughness and point vacancies used in the simulation. Yet, one may argue that a weak tunneling effect presented in the case with surface roughness modulated by $\delta h = 1.0$ nm and $\xi = 20$ nm [Fig. 2(a)] can result in a channel-length dependent β. However, this case is only included as a marginal case to show the strong scattering effect of surface roughness considering that twice of δh could reduce the sample thickness to 1.6 nm.

Based on the combined resistivity from 2% point vacancies and surface roughness, a 3.7-nm mean free path can be obtained for the 3.6-nm-thick sample in the presence of a rough surface with $\delta h = 0.8$ nm and $\xi = 20$ nm, which is comparable to the experimental measurement [4]. Notice that both spin and momentum relaxation rates are smaller in the presence of point vacancies than line vacancies, which is expected as the vacancies along the traverse direction enhance the electron reflections and spin-flip events. As shown in Table III, the resistivity with the presences of both surface roughness and point vacancies is the sum of the resistivity from each individual source, i.e., $\rho_{\text{pt.vac.+surf.}} \approx \rho_{\text{pt.vac.}} + \rho_{\text{surf.}}$, which is consistent with Matthiessen's rule within 5%. Compared to the resistivity induced by surface roughness, under reasonable assumptions, vacancy scattering is dominant over surface scattering for momentum relaxation. As shown in Table IV, a linear vacancy concentration dependence is found
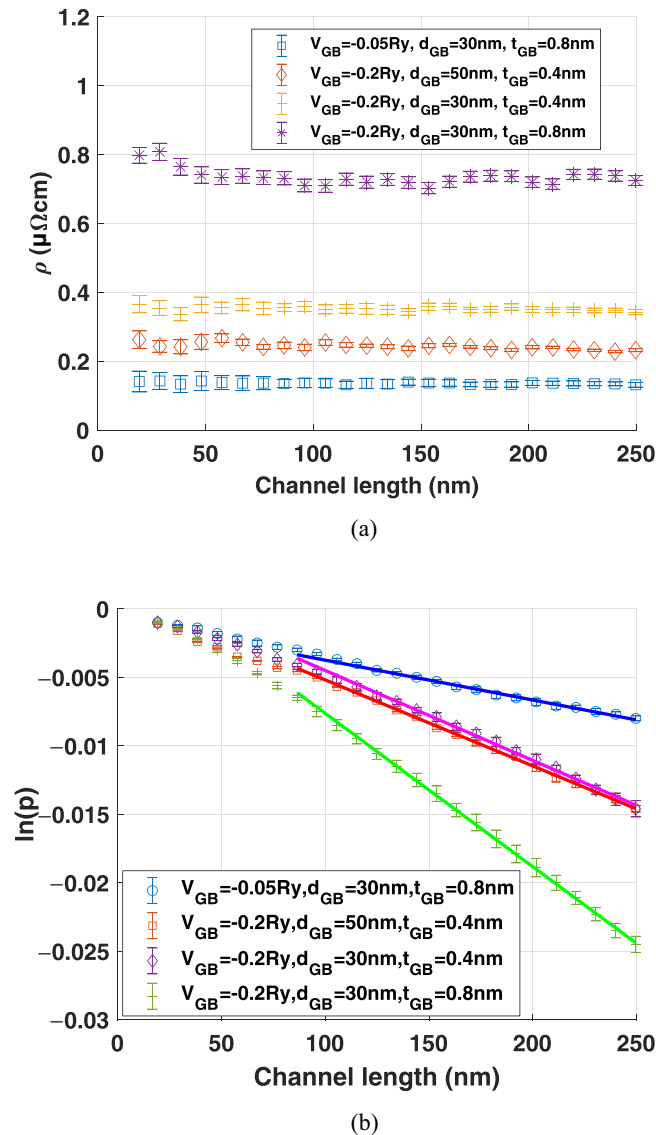

FIG. 4. (a) Resistivity of 3.6-nm-thick film vs channel length for different grain boundary parameters. (b) Spin diffusion lengths for a 3.6-nm-thick channel under the same sets of grain boundary parameters as above.
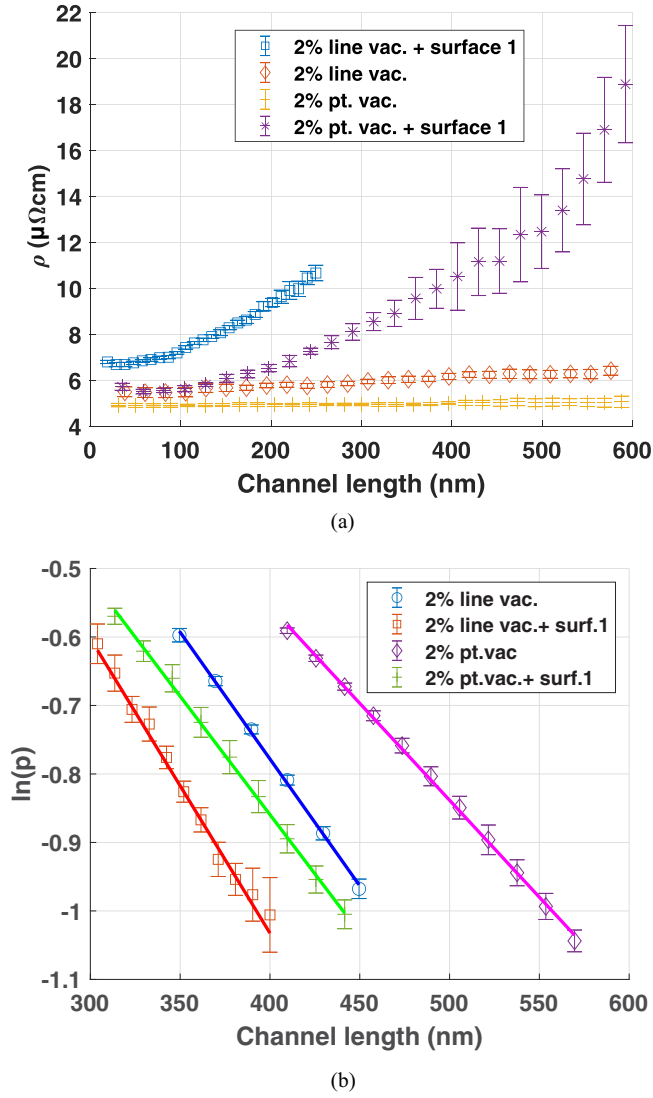
(a)

(b)

FIG. 5. (a) Resistivity of 3.6-nm-thick film vs channel length with 2% line vacancies (with surf.1) in purple (blue) and 2% point vacancies (with surf.1) in yellow (red); surface 1 is modulated by $\delta h = 0.8$ nm and $\xi = 20$ nm. Note that the case with the 2% line vacancies and surface 1 is only plotted to 250 nm because the strong tunneling effect makes the transmission function too small to acquire an accurate resistivity. (b) Spin diffusion lengths for a 3.6-nm-thick channel under the same condition as above.

in ρ_{vac} when the vacancy concentration is below 1.0%, which can also be predicted analytically from the Green's function method as in Ref. [51]. In the diffusive regime, resistivity is inversely proportional to the product of the channel number M across the Fermi level and an ensemble average transmission function T. For a system with uniformly and independently distributed vacancies of a concentration C_{vac}, the correlation function for the vacancy scattering potential Δ between any two sites is

$$\langle \Delta_{i,n,s} \Delta_{i',n',s'} \rangle = \delta_{i,i'} \delta_{n,n'} \delta_{s,s'} \left(C_{\mathrm{vac}} \Delta^2 - C_{\mathrm{vac}}^2 \Delta^2 \right) + C_{\mathrm{vac}}^2 \Delta^2,$$

where i, n, and s are the indices for the position along the transverse and longitudinal directions respectively. Applying Dyson's equation and collecting the terms linear in the chan-

TABLE III. Summary of the effect of 2% vacancies on spin transport in an Al film with 3.6 nm thickness at $T = 0$ K.

Relaxation mechanism	ρ ($\mu \Omega$ cm)	L_{sd} (nm)	β_{vac}
line vacancies	nonohmic	270	-
line vac. + surf.1[a]	nonohmic	233	-
point vacancies	4.95	353	6400
point vac. + surf.1	5.83	290	6000

[a]Surface roughness modulated by $\delta h = 0.8$ nm and $\xi = 20$ nm.

nel length L, the reflection amplitude

$$\langle |r_{k,k'}|^2 \rangle = L \sum_{n,s} C_{\mathrm{vac}} (1 - C_{\mathrm{vac}}) \Delta^2$$

$$\times [|\phi_k(n,s)|^2 |\phi_{k'}(n,s)|^2 / v_k v_{k'}],$$

where k denotes the transverse mode, v_k is the velocity associated with the k_{th} mode and $\phi_k(n,s)$ denotes the wave function for an electron state $|n, k, s\rangle$. Assuming $\sum_{k,k'} \langle |r_{k,k'}|^2 \rangle \ll 1$ as in the system with dilute vacancies,

$$\rho \propto \sum_{n,s} C_{\mathrm{vac}} (1 - C_{\mathrm{vac}}) \Delta^2 [|\phi_k(n,s)|^2 |\phi_{k'}(n,s)|^2 / v_k v_{k'}].$$

Given that $C_{\mathrm{vac}} \ll 1$, the linear dependence on C_{vac} can be seen. As the linear dependence on the vacancy concentration is derived from the independence of the vacancy distribution, when the vacancy concentration increase above a certain value, the associated scattering potential starts to overlap and interact, causing the deviation from linearity. This deviation from the linear dependence is observed when C_{vac} is above 1.0% as illustrated in Fig. 6 and the better quadratic fitting suggests that the vacancy overlapping matters as C_{vac} increases above 1.0%. Note that the quadratic fitting equation given in the form of $y = 284.2x(1 - 6.56x)$ rather than in the form of $C_{\mathrm{vac}}(1 - C_{\mathrm{vac}})$ as predicted, suggests that the interaction between vacancies is stronger than the prediction and a higher order of expansion in Dyson's equation is required to correctly describe it.

Note that the different effects on the momentum relaxation can be attributed to the nature of isolated defects and clustered defects. The features of surface roughness can be understood as the clusters of multiple vacancies, forming an effective scattering potential locally which is attenuated by the interaction of the local scattering potential associated with each vacancy. Therefore the resulting ρ_{surf} is characterized by $\delta h / \xi$. In contrast, for the system with dilute vacancies, the average intervacancy separation d_{vac} is of comparable magnitude as ξ or longer so that it is safe to consider that each scattering event associated with each isolated vacancy is independent and additive, leading to $\rho_{\mathrm{vac}} \propto C_{\mathrm{vac}}$. Hence, momentum relaxation is

TABLE IV. Summary of resistivity induced by vacancies at $t_N = 3.6$ nm and $T = 0$ K.

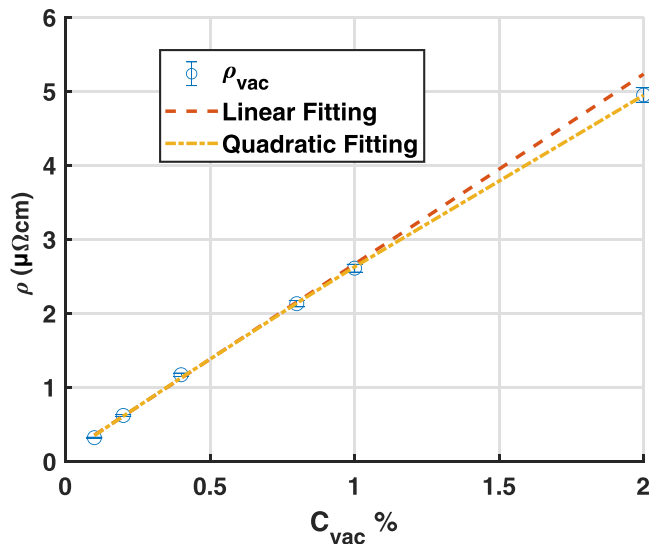| C_{vac}	0.1%	0.2%	0.4%	0.8%	1.0%	2.0%
ρ ($\mu \Omega$ cm)	0.32	0.62	1.17	2.13	2.61	4.95

FIG. 6. Resistivity of 3.6-nm-thick film varies with C_{vac} in blue; the linear fitting on C_{vac} in a red dashed line and the quadratic fitting on C_{vac} in a yellow dashed line with the fitting equation $y = 284.2x(1 - 6.56x)$.

more susceptible to point vacancy than surface roughness in the thin film regime.

As given in Tables III and I, the spin diffusion length due to vacancies is generally ~2 times shorter than that induced by surface roughness at $t_N = 3.6$ nm, while the corresponding resistivity is more than 5 times larger. Consequently, β_{vac} is one order of magnitude larger than β_{surf}. This reflects the difference between bulk and surface defects. Generally, a surface band is narrower than a bulk band within a system which leads to a smaller electron level spacing or an energy gap ΔE. Thus a larger β_{vac} is expected, following $\beta = (\Delta E / \lambda_{SOI})^2$ as predicted by Elliott-Yafet theory. This reflects the energy broadening due to spin flip scattering being suppressed by the surface energy spacing.

D. Surface reconstruction

Spin and momentum relaxation induced by surface reconstruction has also been studied. A repetitive indentation with a given period is repeatedly placed at the top surface to simulate the surface reconstruction, equivalent to 50% missing atoms at the surface. To investigate the combined effect of point vacancies and surface reconstruction, 0.1%, 0.4%, 0.8%, and 1.6% point vacancies are included along with surface reconstruction. It is observed that the presence of surface reconstruction and point vacancies enhance both spin and momentum relaxation and the simulation results become similar to the experimental measurements. Note that constant resistivity is observed as shown in Fig. 7(a). Thus it is accurate to use the resistivity determined at 250 nm as representative to extract β. As shown in Table V, a nearly zero resistivity indicates that electron scattering due to the repetitive surface corrugation is negligible owing to little symmetry breaking in the propagation and transverse directions. The possibility of ballistic transport for periodic surface corrugations cannot
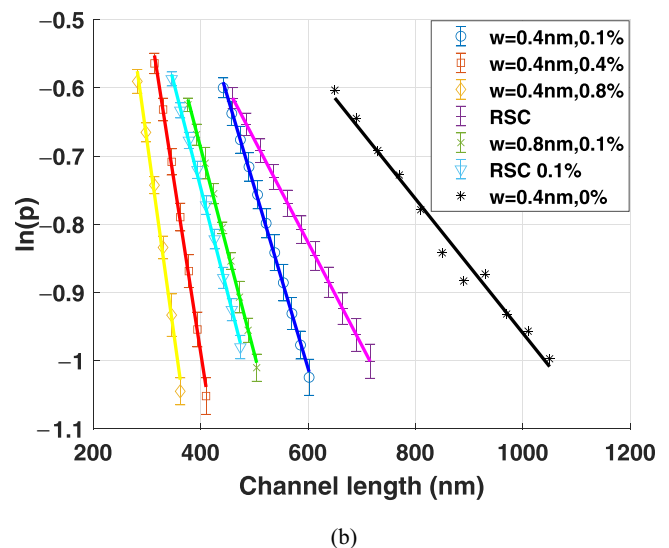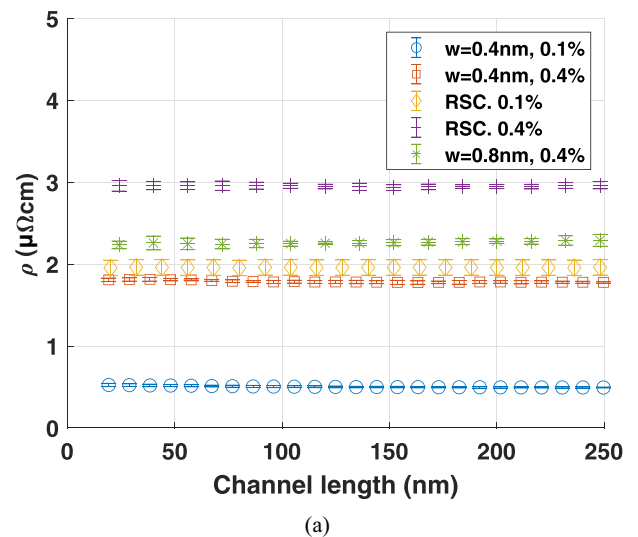

(a)

(b)

FIG. 7. (a) Resistivity of 3.6-nm-thick film versus channel length in the presence of periodic surface corrugations/random surface corrugations and 0.1%, 0.4% point vacancies. (b) Spin diffusion lengths for a 3.6-nm-thick film with varying widths of surface corrugation and varying vacancy concentration.

be ruled out, although the signature trend as demonstrated in Fig. 4 in Ref. [52] is not observed. Given the nearly zero resistivity, the associated spin relaxation can be explained by the Rashba effect [53,54] originating from the symmetry breaking in the thickness direction due to the surface corrugation such that the intraband scattering matrix element is nonzero, i.e., causing the intraband spin scattering.

To investigate the effect of periodicity of surface reconstruction, random corrugations are introduced on the surface to replace the repetitive surface corrugations such that the resulting width of the average surface plateau is 0.8 nm without periodicity. As shown in Table V, in the presence of 0.1% vacancies, comparing the case with 0.8 nm-width repetitive surface corrugation to that with random surface corrugations, the resulting resistivity is increased ~300% from 0.68 to 1.95 $\mu\Omega$ cm but the associated spin diffusion length merely

TABLE V. Summary of the effect of surface reconstruction on electric and spin transport in an Al film with 3.6 nm thickness at $T = 0$ K.

δw (nm)	$C_{\text{vac}}\%$	ρ (μ Ω cm)	L_{sd} (nm)	$\beta_{\text{recon+vac}}$[a]
0.4	0	0.06	1020	7.9
0.4	0.1	0.47	377	66
0.8	0.1	0.68	332	107
0.4	0.4	1.69	198	235
0.8	0.4	2.3	202	443
0.4	0.8	3.02	175	585
0.4	1.6	5.3	166	1620
RSC[b]	0.0	1.39	650	1710
RSC	0.1	1.96	325	850
RSC	0.4	2.96	245	1079
RSC	0.8	3.70	210	1265
RSC	1.6	5.60	190	2371

[a]The extraction of β is based on its definition, which does not necessarily imply EY mechanism is responsible for the derived value.
[b]RSC symbolizes random surface corrugations.

decreases ∼2%. This suggests that the periodicity of surface corrugation breaks the connection between momentum relaxation and spin relaxation as indicated by the change of β in Table V. Surface periodicity effectively mitigates the momentum relaxation owing to symmetry such that the electron momentum corresponding to the width of the surface corrugation is robust against backscattering, leading to a consistently smaller resistivity induced by periodic surface corrugations (PSC) compared to that induced by random surface corrugations (RSC).

In addition, a clear departure from Matthiessen's rule of resistivity is observed. For example, the sum of ρ_{vac} with 0.1% vacancies (from Table IV) and ρ due to random surface corrugation as in line 8 of Table V mispredicts the combined resistivity by ∼15%. In contrast, increasing the concentration of vacancies further breaks the symmetry along the propagation direction, leading to the increase in resistivity and the effective removal of the deviation from Matthiessen's rule. For instance, Matthiessen's rule accurately predicts the resistivity within 5% for the case of 0.8% vacancies and RSC.

Furthermore, the introduction of point vacancies results in further amplification of spin relaxation as shown in Fig. 7(b), which again is attributed to loss of inversion symmetry along the thickness direction and propagation direction. The resulting spin diffusion lengths for the cases with 0.4% vacancies or above are approximately 5 times shorter than the case with periodic surface corrugations alone. Interestingly, 0.1% va-

TABLE VI. Summary of anisotropy of spin transport in an 3.6-nm-thick Al film with 0.4nm periodicity of surface corrugation and 0.8% vacancies or 2% vacancies alone at $T = 0$ K.

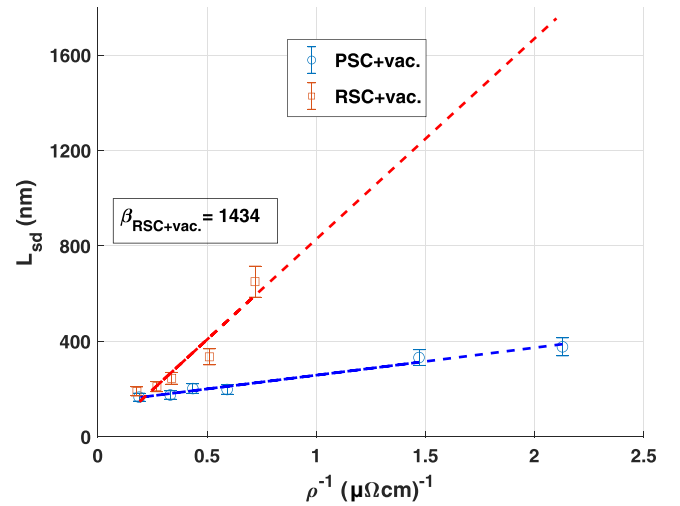|	$w = 0.4$ nm, $C_{\text{vac}} = 0.8\%$	$C_{\text{vac}} = 2.0\%$
$L_{sd,x}$ (nm)	490	492
$L_{sd,y}$ (nm)	207	475
$L_{sd,z}$ (nm)	175	353

FIG. 8. L_{sd} vs ρ^{-1} for all the cases shown in Table V except the case with PSC alone. The fitting equations are $y = 115.2x + 143$ for vacancies and PSC in the blue dash line and $y = 841x - 13.3$ for vacancies and RSC in the red dash line. The associated $\beta_{\text{RSC+vac.}}$ is determined from the slope.

cancies brings about a spin diffusion length 2.5 times shorter (∼1000 to ∼400 nm), but doubling from 0.4% to 0.8% vacancy concentration only decreases the spin diffusion length by ∼10% as shown in Table V. Similar to the enhancement of momentum relaxation owing to the induction of random corrugations, this suggests that the inefficacy of periodic surface corrugations in relaxing spin momentum is easily broken by any kind of randomness in the system, even 0.1% vacancies.

Following EY theory, $L_{\text{sd}} = \sqrt{3\beta}/\rho g(E_F)e^2 v_F^2$. As shown in Fig. 8, a fairly good fitting based on the EY theory in red with a reasonable $\beta_{\text{RSC+vac.}}$ (1434 ± 138) suggests that EY prediction is valid for the cases with RSC. However, for the cases with PSC and vacancies, the presence of the positive constant term in the blue dash line violates the EY mechanism which predicts a linear relation between L_{sd} and ρ^{-1} with a constant β and a zero constant term. This can be attributed to the different responses to the symmetry breaking between momentum relaxation and spin relaxation, which closely depends on the scattering length scale and concentration of random defects. In the presence of PSC, the length scale associated with symmetry breaking is determined by the average distance of vacancy separation, which is comparable or longer than the typical length of momentum relaxation (∼10 nm) depending on the vacancy concentration. Thus symmetry can be better preserved at the typical scattering length of momentum relaxation (∼10 nm) than that at the typical length of spin relaxation (∼300 nm) such that electron transport within the typical length of momentum relaxation is nearly ballistic owing to PSC, while the spin transport between the spin scatterings is diffusive.

In contrast, the introduction of random surface corrugations breaks the translational symmetry at a much smaller length scale such that symmetry breaking is comparable at both length scales of momentum relaxation and spin relaxation. Note that the positive correlation between $\beta_{\text{PSC+vac.}}$ and C_{vac} as shown in Table V could indicate that as the vacancy

TABLE VII. Summary of the experimental results on spin transport in Al-NLSV at $T = 4$ K (adapted from Ref. [17]).

t_N (nm)	ρ ($\mu \Omega$ cm)	L_{sd} (nm)	β	Ref.
6	33.3	200	9.0×10^4	42
8.5	9.5	70	700	4
10	9.1	420	2.95×10^4	42
12	9.52	455	3.80×10^4	43
15	2.5	660	0.55×10^4	44
20	5.2	450	1.11×10^4	45
20	4	850	2.34×10^4	46

concentration increases, a non constant β is attributed to the reduced contribution of surface spin-flip scattering [55], which has a larger spin-flip probability ($1/\beta$) than that of bulk scattering. This is still inconclusive, however, as separating surface scattering from bulk scattering cannot be achieved accurately, limited by the departure from Matthiessen's rule. In addition, a clear overlap is observed between PSC and RSC at a larger vacancy concentration shown in Fig. 8, suggesting the Elliott-Yafet prediction is expected to recover when the bulk scattering dominates. This is also indicated by the relatively small difference between $\beta_{1.6\%,\text{PSC}}$ (1620) and $\beta_{1.6\%,\text{RSC}}$ (2371).

Compared to the cases with the presence of both surface roughness and 2% point vacancies, the combined effect of point vacancies and 0.4nm-width surface corrugations gives rise to ~2 times shorter spin diffusion length and therefore approximately one order of magnitude smaller β when the associated resistivities are of comparable magnitude.

Although surface corrugation is a special case of surface reconstructions, it reflects the significance of periodicity in momentum and spin relaxation, which can be extended to other surface reconstructions that have localized periodicity.

E. Anisotropy of spin relaxation

So far, spin relaxation has been studied for the spins along z direction, i.e., thickness direction as shown in Fig. 1. By rotating the spin basis of H_{so} to transverse directions, anisotropic spin relaxation is explored with two representative cases: A system with surface corrugations with the periodicity of 0.4 nm and 0.8% point vacancies and a system with 2% vacancies. As shown in Table VI, clearly the largest difference in spin diffusion lengths distinguishes the x direction (direction of surface corrugation periodicity) from the others. It is traceable to the surface corrugations: it vanishes within the film plane (x and y directions) when the corrugation is removed. There is also a second smaller anisotropy between the direction perpendicular to the plane (z) and parallel to the plane as one would expect from Rashba arguments as presented in Ref. [56]. The spin diffusion length for x spins is always found to be the largest, in qualitative agreement with the experimental Ref. [56] which, however, has edge effects not included in the periodically connected thin film used in this work.

F. Spin hot spots

To check the effect of spin hot spots, the variation of spin polarization with respect to the k vectors in the presence of surface roughness is examined. The outliers in spin polarization appear in a ratio of 1/20. The total transmission for the outliers are about half of that for regular k points. This implies that even for the 50% mixing of spin when $P = 0$, the removal of those outliers will only increase P by ~5%. Thus the inclusion of those outliers does not contribute much to the spin flip scattering that significantly changes an order of magnitude of spin relaxation time. It makes sense because the presence of surface roughness breaks the space inversion symmetry and removes the contribution of spin hot spots as it effectively lifts the degeneracy of spin states and makes the band structure around the Fermi level smoother. Similarly, other defects which serve to break the space inversion symmetry can also smear out the spin hot spots, such as grain boundary, vacancies or surface corrugation.

IV. CONCLUSION

In this paper, the effects of surface roughness, GB scattering, vacancies and surface reconstruction on the momentum and spin relaxation are investigated in a Al thin film with $t_N = 3.6$ nm at $T = 0$ K. Point vacancies are found to be the dominant contribution to the momentum relaxation as the resulting resistivity is similar to experimental measurements, while the resistivity induced by the other defects are at least one order of magnitude smaller. Spin relaxation is dominated by the combined effect of surface reconstruction and point vacancies, which leads to $L_{sd} = \sim 200$ nm and $\beta \leqslant 1000$ with a reasonable assumption of vacancy concentration.

It has been observed that the presence of surface corrugation results in a clear departure from Matthiessen's rule. The violation of the EY prediction for β is found in the presence of periodic surface corrugations and vacancies. This is attributed to the different responses to symmetry breaking between momentum relaxation and spin relaxation as symmetry breaking is not comparable at both length scales of momentum and spin. In addition, a strong anisotropy of spin relaxation for the spins parallel to the propagation direction is found, relevant to surface corrugations.

It has been found that the spin diffusion length induced by surface roughness is proportional to $(\delta h / \xi)^{-1/2}$ as opposed to $(\delta h / \xi)^{-1}$, which can be attributed to the interference between multiple surface features. A linear vacancy concentration dependence is found for resistivity when the vacancy concentration is below 1.0% and a departure from linearity is attributed to the interaction between the vacancy scattering potentials.

[1] T. Kimura, T. Sato, and Y. Otani, Phys. Rev. Lett. **100**, 066602 (2008).

[2] F. J. Jedema, A. T. Filip, and B. J. van Wees, Nature **410**, 345 (2001).

[3] H. Zou and Y. Ji, Appl. Phys. Lett. **101**, 082401 (2012).

[4] J. D. Watts, Ph.D. thesis, University of Minnesota-Twin Cities (2018), retrieved from the University of Minnesota Digital Conservancy, https://hdl.handle.net/11299/202195

[5] R. L. Graham, G. B. Alers, T. Mountsier, N. Shamma, S. Dhuey, S. Cabrini, R. H. Geiss, D. T. Read, and S. Peddeti, Appl. Phys. Lett. **96**, 042116 (2010).

[6] A. Vogel, J. Wulfhorst, and G. Meier, Appl. Phys. Lett. **94**, 122510 (2009).

[7] F. J. Jedema, M. S. Nijboer, A. T. Filip, and B. J. van Wees, Phys. Rev. B **67**, 085319 (2003).

[8] H. Idzuchi, Y. Fukuma, and Y. Otani, Physica E **68**, 239 (2015).

[9] A. Vedyayev, N. Ryzhanova, N. Strelkov, T. Andrianov, A. Lobachev, and B. Dieny, Phys. Rev. Appl. **10**, 064047 (2018).

[10] M. N. Baibich, J.M. Broto, A.Fert, F. Nguyen. Van Dau, F. Petroff, P. Etienne, G. Creuzet, A. Friederich, and J. Chazelas, Phys. Rev. Lett. **61**, 2472 (1988).

[11] G. Binasch, P.Grunberg, F. Saurenbach, and W. Zinn, Phys. Rev. B **39**, 4828 (1989).

[12] S. Roche and S. O. Valenzuela, J. Phys. D: Appl. Phys. **47**, 094011 (2014).

[13] S. B. Touski and M. Pourfath, Appl. Phys. Lett. **103**, 143506 (2013).

[14] S. B. Touski, R. Roldan, M. Pourfath, and M. Pilar Lopez-Sancho, Phys. Rev. B **95**, 165301 (2017).

[15] G. Mihajlovic, J. E. Pearson, S. D. Bader, and A. Hoffmann, Phys. Rev. Lett. **104**, 237202 (2010).

[16] E. Villamor, M. Isasa, L. E. Hueso, and F. Casanova, Phys. Rev. B **87**, 094417 (2013).

[17] S. Rakheja, S.-C. Chang, and A. Naeemi, IEEE Trans. Electron Devices **60**, 3913 (2013).

[18] A. Matthiessen and C. Vogt, Ann. Phys. **198**, 19 (1864).

[19] C. Kittel, *Introduction to Solid State Physics* (Wiley, New York, 1996).

[20] R. Elliott, Phys. Rev. **96**, 266 (1954).

[21] Y. Yafet, Phys. Rev. **85**, 478 (1952).

[22] Y. Yafet, in *Solid State Physics*, edited by F. Seitz and D. Turnbull (Academic Press, New York, 1963).

[23] K. Moors, B. Sorée, Z. Tökei, and W. Magnus, J. Appl. Phys. **116**, 063714 (2014).

[24] K. Fuchs, Math. Proc. Cambridge Philos. Soc. **34**, 100 (1938).

[25] E. H. Sondheimer, Adv. Phys. **1**, 1 (1952).

[26] A. F. Mayadas and M. Shatzkes, Phys. Rev. B **1**, 1382 (1970).

[27] Y. Shim, V. Borovikov, B. P. Uberuaga, A. F. Voter, and J. G. Amar, Phys. Rev. Lett. **101**, 116101 (2008).

[28] M. W. Finnis and V. Heine, J. Phys. F: Met. Phys. **4**, L37 (1974).

[29] W. Gruber, S. Chakravarty, C. Baehtz, W. Leitenberger, M. Bruns, A. Kobler, C. Kubel, and H. Schmidt, Phys. Rev. Lett. **107**, 265501 (2011).

[30] J. Fabian and S. Das Sarma, Phys. Rev. Lett. **81**, 5624 (1998).

[31] J. Fabian and S. Das Sarma, Phys. Rev. Lett. **83**, 1211 (1999).

[32] R. Landauer, Philos. Mag. **21**, 863 (1970).

[33] M. Büttiker, Phys. Rev. Lett. **57**, 1761 (1986).

[34] W. A. Harrison, *Elementary Electronic Structure* (World Scientific, Singapore, 1999).

[35] D. A. Papaconstantopoulos, *Handbook of the Band Structure of Elemental Solids* (Plenum, New York, 1986).

[36] C. Caroli, R. Combescot, P. Nozieres, and D. Saint-James, J. Phys. C: Solid State Phys. **4**, 916 (1971).

[37] M. P. Lopez Sancho, J. M. Lopez Sancho, J. M. L. Sancho, and J. Rubio, J. Phys. F: Met. Phys. **15**, 851 (1985).

[38] L. Kiss, J. Söderlund, G. Niklasson, and C. Granqvist, Nanotechnology **10**, 25 (1999).

[39] N. W. Ashcroft and N. D. Mermin, *Solid State Physics* (Holt, Rinehart and Winston, New York, 1976).

[40] P. Y. Zhang, T. Zhou, B. Engler, J. Chawla, R. Hull, and D. Gall, J. Appl. Phys. **122**, 095304 (2017).

[41] P. Prange and T.-W. Nee, Phys. Rev. **168**, 779 (1968).

[42] S. Valenzuela and M. Tinkham, Appl. Phys. Lett. **85**, 5914 (2004).

[43] S. Valenzuela and M. Tinkham, Nature **442**, 176 (2006).

[44] N. Poli, M. Urech, V. Korenivski, and D. Haviland, J. Appl. Phys. **99**, 08H701 (2006).

[45] C. H. L. Quay, D. Chevallier, C. Bena, and M. Aprili, Nat. Phys. **9**, 84 (2013).

[46] M. Urech, V. Korenivski, N. Poli, and D. Haviland, Nano Lett. **6**, 871 (2006).

[47] M. Yamamoto, T. Matsumae, Y. Kurashima, H. Takagi, T. Suga, S. Takamatsu, T. Itoh, and E. Higurashi, Micromachines **11**, 454 (2020).

[48] Z. Q. Chen, W. C. Tian, X. T. Zhang, and Y. K. Wang, J. Micromech. Microeng. **27**, 113003 (2017).

[49] J. Ding, D. Neffati, Q. Li, R. Su, J. Li, S. Xue, Z. Zhang, Y. Zhang, H. Wang, Y. Kulkarni, and X. Zhang, Nanoscale **11**, 23449 (2019).

[50] J. Mäkinen *et al.*, Surf. Sci. **175**, 385 (1986).

[51] X. Chen and R. H. Victora, Appl. Phys. Lett. **93**, 162105 (2008).

[52] P. Esquinazi, J. Barzola-Quiquia, S. Dusari, and N. García, J. Appl. Phys. **111**, 033709 (2012).

[53] E. I. Rashba, Sov. Phys. Solid State **2**, 1109 (1960).

[54] Y. A. Bychkov and E. I. Rashba, JETP Lett. **39**, 78 (1984).

[55] Y. J. Cai, C. Qin, F. Kandaz, X. Y. Shen, C. Zhou, M. W. Jia, Y. M. Luo, Y. Z. Wu, and Y. Ji, Phys. Rev. B **100**, 144419 (2019).

[56] C. Zhou, F. Kandaz, Y. J. Cai, C. Qin, M. W. Jia, Z. Yuan, Y. Z. Wu, and Y. Ji, Phys. Rev. B **96**, 094413 (2017).